Enhancing Selectivity in 5G/6G Ultra-Narrowband Applications: Plug-and-Play Frequency Selective Surfaces with Field-Manipulating Vias

Jaehoon Kim, *Student Member, IEEE,* Seungwoo Bang, *Student Member, IEEE,* Jungi Jeong, *Member, IEEE,* Sang-Hyuk Wi, *Member, IEEE* and Jungsuek Oh, *Senior Member, IEEE*

***Abstract*— This study presents unmatchedly selective ultra-narrowband frequency selective surfaces (FSSs) for a pioneering external RF front-end (RFFE) filtering solution integrated with diverse beamforming antenna modules. The limitations of current base station filters for 28 GHz are demonstrated, and an inventive approach that extends the boundaries of the filtering block by positioning it outside the RFFE for spatial reinforcement is newly devised. An innovative analysis of narrow-bandpass complementary resonator pairs are introduced, unlocking unprecedented selectivity by addressing the challenging issue of recalcitrant mutual coupling arising from a dispersive field distribution. This spatial methodology extends the frontier by seamlessly integrating field analysis with a mixed coupling theory previously established in the circuit domain. Subsequently, an trailblazing technique is proposed for precise control of coupling balance, utilizing field-manipulating vias to centralize the primary current in the complementary resonator. This approach achieves an average rejection of 60 dB across the stopband, ensuring robust stability for incident angles up to 70°, surpassing previous counterparts. Furthermore, it demonstrates a significantly improved roll-off in the transition band and achieves a remarkable 2.7% bandwidth, comparable to the 850 MHz for the n261 band of 5G NR.**

***Index Terms*— Complementary resonator, frequency selective surface, mixed coupling, narrowband, out-of-band rejection, roll-off.**

I. Introduction

The evolution of fifth-generation (5G) involves utilizing millimeter-wave (mmWave) frequencies above 28 GHz, offering a substantial increase in bandwidth (BW) [1]. However, coverage limitations arise due to increased loss and reduced propagation reach. Extensive research is addressing these challenges with novel technologies not employed in earlier generations [2], [3], [4]. Among these, extreme massive multiple-input and multiple-output (X-MIMO) emerges as a core technology for boosting capacity [5]. X-MIMO deploys thousands or even tens of thousands of antennas, presenting new design challenges compared to pre-5G base stations. The increasing frequency reduces MIMO element size, necessitating a compact RF front-end (RFFE) architecture with high integration density. However, filters designed for sub-6 GHz face challenges in compact integration when applied to mmWave [6], [7]. Thus, research on miniaturized microstrip filters is actively explored as an alternative [8], [9]. However, their performances, including quality factor (Q), still lag behind existing solutions. As MIMO elements increase, the required out-of-band rejection grows proportionally [10]. Additionally, minimizing interference at the early stages of receiver chains is a favorable approach for MIMO objectives, enhancing interference robustness and reducing power consumption concurrently. Hence, plug-and-play frequency selective surfaces (FSSs) that are easily integrated with beamforming modules can mitigate the impediment associated with traditional RFFE filters at the external interface, while spatially enhancing the signal-to-noise ratio (SNR). However, most previous studies fail to meet the narrowband requirement for 5G, around 800 MHz (2.8% at 28 GHz), set by 3GPP. Moreover, the robustness of critical parameters is damaged under wide angles of incidence for transverse electric (TE) and magnetic (TM) waves.

Numerous studies aimed to develop highly selective narrowband FSSs [11], [12], [13], [14], [15], [16], [17]. While [11] achieved relative narrowband using a single PCB, a limited roll-off is attained. [12] and [13] achieved a low insertion loss (IL) and improved roll-off with higher-order response. However, a critical drawback emerged: the passband frequency spaced out as the incident angle increased. [14] and [15] reported improved rejection but with limited BW and angular stability. [16] reported a BW narrower than targeted 2.8% but faced challenges in angular stability and fabrication complexity. While [17] achieved enhanced selectivity through coupling, its rejection is constrained by topological limitations. Moreover, narrowing the BW necessitates compromises in terms of IL and out-of-band rejection.

This study introduces an efficacious methodology that independently enhances stopband rejection without compromising the passband and roll-off response, representing a substantial leap forward in achieving superior preselecting performance. The remainder of the paper is as follows: In Section II, we systematically advance the analysis of electromagnetic (EM) coupling using complementary narrow-bandpass resonators to achieve unmatched selectivity and ultra-narrowband characteristics. Subsequently, field-manipulating vias are proposed, serving the tri-purpose of generating transmission zeros (TZs) on both transition bands (skirts) to maintain balanced roll-off, greatly improving out-of-band rejection through inductance optimization, and converging internal fields for robust angular stability. In Section III, simulated and measured results of the FSSs are presented. Finally, Section IV provides the conclusion.

II. Unit Cell Analysis for Exceptional Selectivity and Ultra-Narrowband

This section proposes the unit cell (UC) topology for the FSS, followed by circuit modeling. Numerical simulations are validated through correspondence with the mixed coupling theory and field analysis using full-wave EM simulations [18]. Moreover, an inventive methodology to achieve an extremely selective ultra-narrowband response with excellent angular stability is newly introduced.

A. Complementary Resonators with Coupling Apertures

Fig. 1(a) shows the complementary four-legged loop topology for narrowband response. The proposed configuration, with its four

This work was supported by SAMSUNG Research, Samsung Electronics Co., Ltd. (*Corresponding author: Jungsuek Oh*).

Jaehoon Kim, Seungwoo Bang and Jungsuek Oh are with the School of Electrical and Computer Engineering, Institute of New Media and Communications (INMC), Seoul National University, Seoul 152-742, South Korea (e-mail: jaehoonkim@snu.ac.kr; littlebang97@snu.ac.kr; jungsuek@snu.ac.kr).

Jungi Jeong and Sang-hyuk Wi are with the Samsung Research, Seoul 06765, South Korea (e-mail: jungi.jeong@samsung.com; sang-hyuk.wi@samsung.com).

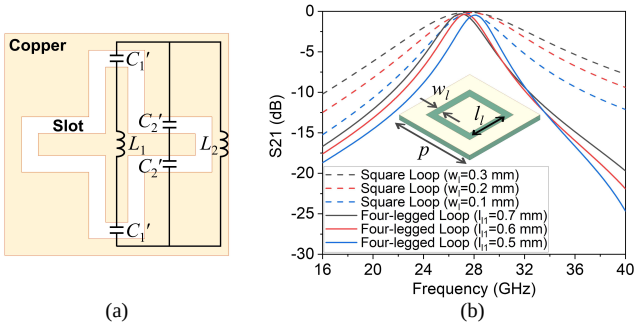

(a) (b)

Fig. 1. (a) Complementary four-legged loop topology and (b) Floquet $|S_{21}|$ of UCs with square and four-legged loop resonators for w_l and l_{l1} values.

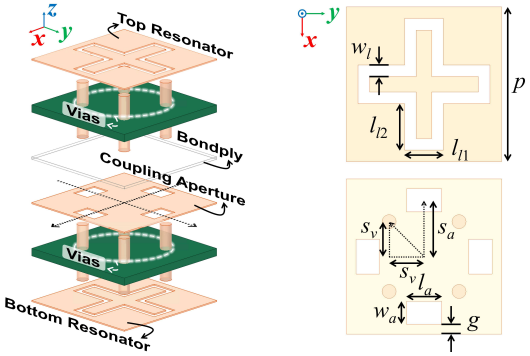

(a) (b)

Fig. 2. (a) Exploded view of complementary four-legged loop-loaded aperture coupled UC and (b) top views of constituent resonators and coupling apertures.

vertices of the square loop directed inward toward the center, offers enhanced Q compared to the square loop. Fig. 1(b) shows the Floquet $|S_{21}|$ of UCs with square and four-legged loop resonators. Ansys High-Frequency Structure Simulator (HFSS) was used for EM simulations. Both UCs consist of a substrate with a resonator on top. The substrates are RF-35 from Taconic, with a dielectric constant of 3.5, a loss tangent of 0.0018, and a thickness of 0.25 mm. The top resonator with design parameters represents a complementary square loop configuration. The value of p and l_l are 4 and 2.1 mm, respectively. The design parameters of the proposed four-legged loop are defined in the top drawing of Fig. 2(b). The values of the corresponding parameters are as follows: p=4 mm, w_l=0.2 mm, l_{l1}=0.7 mm, l_{l2}=1.05 mm. As indicated in Fig. 1(b), the square loop constrains the achievable Q for w_l. Additionally, the minimum etching size of the standard PCB process further limits its value. In contrast, the four-legged loop exhibits a narrower passband and higher selectivity with identical resonant length and loop width (w_l). The enhancement, especially as l_{l1} decreases, has been confirmed through EM simulation.

To achieve a narrower and more selective response, higher-order characteristics are required, necessitating multiple resonators. However, continuous cascading of resonators results in high IL and limits the low profile of the UC, compromising angular stability. On the other hand, generating TZs without additional resonators effectively achieves a more selective narrowband response [19]. Fig. 2 shows the exploded view of a complementary four-legged loop-loaded aperture coupled UC and top views of constituent resonators and coupling apertures. Fig. 3 synthesizes the corresponding equivalent circuit, incorporating mutual capacitance (C_m) and inductance (L_m) to represent the mixed coupling path. Taconic's Tacbond 1.5, with a thickness of 0.04 mm, was used to bond the two PCBs. Due to its thinness compared to the wavelength, it is ignored in circuit modeling. The free space is modeled as a transmission line with a characteristic impedance of Z_0 (377 Ω). Each substrate is represented as a transmission line with a length (l_{sub}) equal to the substrate's thickness

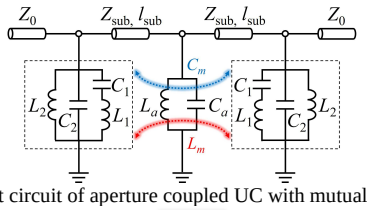

Fig. 3. Equivalent circuit of aperture coupled UC with mutual coupling.

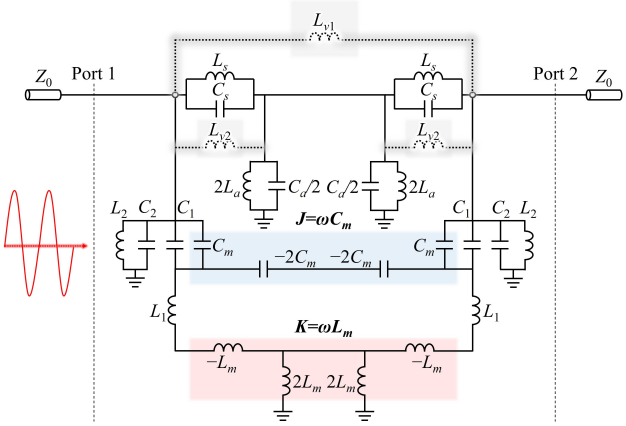

Fig. 4. Alternative form of Fig. 3 with applicable field-manipulating vias.

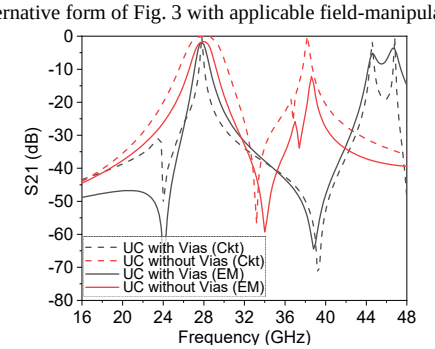

Fig. 5. Simulated $|S_{21}|$ of UCs with and without vias in Fig. 2(a).

TABLE I
CIRCUIT PARAMETERS AND THEIR VALUES WITHOUT VIAS IN FIG. 4

L_1	C_1	L_2	C_2	L_a	C_a	L_m	C_m	L_s	C_s	L_{v1}	L_{v2}
3.5	0.0003	7.1	0.04	0.006	3.22	15.8	0.0015	0.36	0.06	-	-

[Units: nH (Inductance), pF (Capacitance)]

(0.25 mm) and characterized by the impedance Z_{sub}, which accounts for the substrate's dielectric constant of 3.5. The resonators are modeled as shown in Fig. 1(a), and the coupling apertures are represented with shunt inductance (L_a) and capacitance (C_a). Note that the apertures are positioned near the edges of the four legs of the resonator, where the electric field intensity of the resonators is maximum. To achieve an electric field (E)-dominant response, the magnitude of the electric coupling coefficient must exceed that of the magnetic coupling coefficient, enabling the distribution of two TZs at the lower and upper skirts for balanced selectivity compared to magnetic field (H)-dominant response [18]. The mutual components in Fig. 3 can be represented as immittance inverters for a narrowband basis [20], and the transmission lines with interlayer coupling can be treated as shunt L-C circuits, as illustrated in Fig. 4 [21]. The components labeled L_{v1} and L_{v2} which corresponds to the vias in Fig. 2(a) will be detailed in the following sections. At this stage, they are not modelled and considered as open circuits. The circuit and EM simulations of the proposed UC are shown in the red lines in Fig. 5. The corresponding circuit parameters are shown in Table I. In this study, all circuit parameters are determined using the curve-fitting method. Note that unintended H-dominant response generates TZs

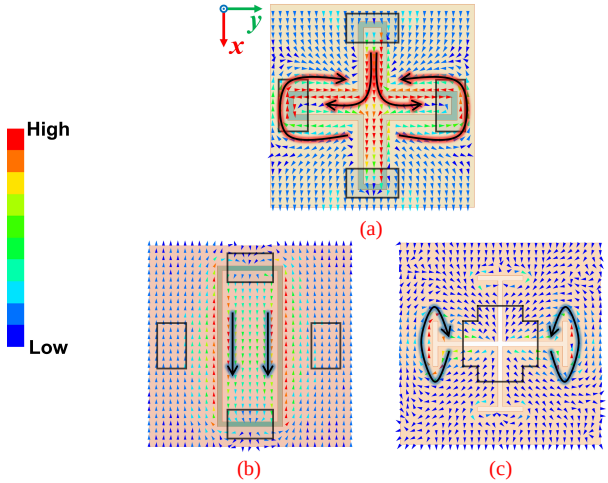

Fig. 6. Surface current vectors of UCs with complementary (a) four-legged loop, (b) squeezed loop, and (c) Jerusalem cross resonators under *x*-pol incidence.

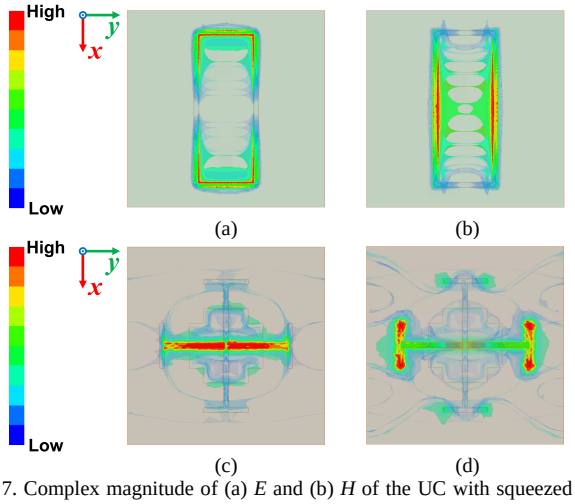

Fig. 7. Complex magnitude of (a) *E* and (b) *H* of the UC with squeezed loop resonators, and (c) *E* and (d) *H* with Jerusalem cross resonators in dielectric substrates under *x*-pol incidence.

only at the upper skirt, despite the arrangement of apertures for an *E*-dominant coupling. Fig. 6(a) illustrates the surface current vector of the four-legged loop resonators under *x*-polarization (pol) incidence, providing insights into the causality of the *H*-dominant response. The desired response is to induce a dominant current exclusively in the upper and lower two legs parallel to the *x*-axis. This minimizes magnetic coupling by creating a current maximum in the central region where the coupling aperture is absent. However, due to the universal fundamentals of the complementary resonator, which has non-localized current paths, dominant current flows along the edges of the two legs parallel to the *y*-axis. This results in strong magnetic coupling at the apertures for *y*-pol. Fig. 6(b) shows the surface current vector of the UC with squeezed loop resonators, designed to confirm the feasibility of achieving an *E*-dominant response with reduced magnetic coupling. The corresponding $|S_{21}|$ is shown as the black solid line in Fig. 8. As anticipated, eliminating the current path into the *y*-pol apertures reduces magnetic coupling and generates a TZ at the lower skirt. Nevertheless, note that this design approach disrupt structural symmetry for dual-pol. In Fig. 6(c), the surface current vector of a UC features another bandpass candidate with complementary Jerusalem cross pairs, creating a localized dominant current path strategically placed away from the central aperture with a symmetric topology. Unlike the normal cross, the Jerusalem topology achieves an *E*-dominant response by cornering the dominant current to the outer

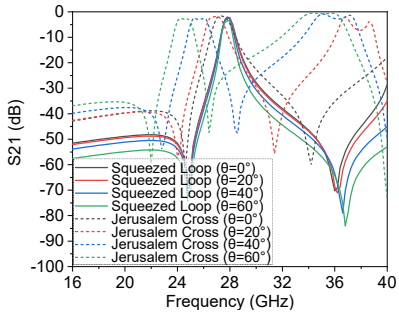

Fig. 8. Simulated $|S_{21}|$ of UCs with complementary squeezed loop and Jerusalem cross resonators under TE incidence.

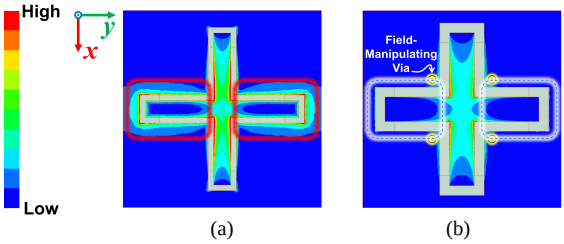

Fig. 9. Complex magnitude of surface current (a) without and (b) with field-manipulating vias on resonators under *x*-pol incidence.

arm, increasing the distance from the aperture. Fig. 7 shows the complex magnitude of *E* and *H* of the UC with squeezed loop and Jerusalem cross resonators in dielectric substrates. Both topologies exhibit a strong *E* region in the aperture and a strong *H* region in the non-aperture area. However, a notable distinction arises as the dominant current localizes to the center or disperses outward. The squeezed loop has a dipole-like field distribution with minimal extension beyond the resonator area. In contrast, the Jerusalem cross exhibits a slot-like distribution, extending the field beyond the resonator and inducing a strong field between adjacent UCs. Put differently, the dipole-like topology, with a smaller effective period than the slot-like topology, minimizes interference with adjacent UCs, ensuring robustness to incident angles [22]. Fig. 8 shows the $|S_{21}|$ of the two UCs for TE incidence, highlighting the superior angular stability of the UC with centralized current. The UC with Jerusalem cross resonators significantly degrades $|S_{21}|$ as the incident angle increases. Omitted for brevity, the four-legged loop topology shifts the passband away from the target frequency as the incident angle increases in a similar manner. Thus, in the following, a simple yet powerful design methodology is introduced that achieves centralized current distribution with a symmetric four-legged loop topology, ensuring an *E*-dominant response and robust angular stability.

B. Field-Manipulating Vias

Herein, an inventive UC topology with field-manipulating vias is proposed that successfully suppresses outward current, achieving a dipole-like field distribution. The newly designed UC is achieved through a straightforward modification, where four additional vias penetrate all three metal layers of the existing UC, as illustrated in Fig. 2(a). The deployment of vias and their parameters are shown in the bottom drawing of Fig. 2(b), with a diameter of 0.15 mm. Fig. 9 shows the complex magnitude of the surface current induced in the UC's resonators under *x*-pol incidence, illustrating the effect of field-manipulating vias. In the UC without field-manipulating vias, strong outward currents are observed at the apertures for *y*-pol. On the other hand, in the UC with the application of field-manipulating vias, a strong current is induced only in the direction parallel to the *x*-axis, as intended for achieving an *E*-dominant response. Additionally, a current maximum is centralized, leading to a dipole-like distribution.

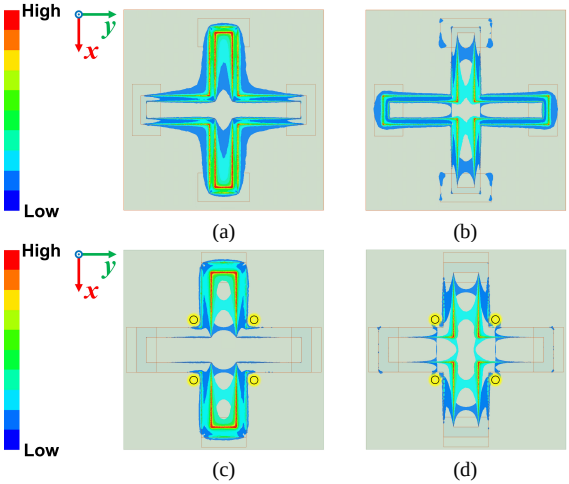

Fig. 10. Complex magnitude of (a) E and (b) H without vias, and (c) E and (d) H with vias in dielectric substrates under x-pol incidence.

TABLE II
CIRCUIT PARAMETERS AND THEIR VALUES WITH VIAS IN FIG. 4

L_1	C_1	L_2	C_2	L_a	C_a	L_m	C_m	L_s	C_s	L_{v1}	L_{v2}
4.08	0.0031	7	0.01	0.01	3.14	0.72	0.0059	0.36	0.55	0.34	0.238

[Units: nH (Inductance), pF (Capacitance)]

Fig. 10 shows the complex magnitude of the E and H induced in the substrates of UCs under x-pol incidence, highlighting the effect of field-manipulating vias. The spread of H to the y-pol apertures, as shown in Fig. 10(b), is effectively reduced, as illustrated in Fig. 10(d). Furthermore, the slight divergence of E in the y-pol apertures, as depicted in Fig. 10(a), is confined solely to the x-pol direction, as shown in Fig. 10(c). Note that this successful isolation of the induced field for each pol greatly simplifies the independent analysis of EM coupling for each incident pol. The circuit and EM simulations of the proposed UC with field-manipulating vias are shown in the black lines in Fig. 5. The corresponding circuit parameters are shown in Table II. As expected, TZs are generated at both the lower and upper edges of the passband. Additionally, the roll-off of the lower skirt is significantly improved compared to that of UCs without vias, leading to a reduction in BW using only a second-order topology. However, note that the higher-order mode around 46 GHz deteriorates wide out-of-band rejection. In the following, via inductance optimization is performed to reinforce the upper band out-of-band rejection.

C. Via Optimization for Enhanced Out-of-band Rejection

Here, the changes in the frequency response of UCs with respect to the inductance of field-manipulating vias is analyzed to achieve wide out-of-band rejection. The dashed lines in Fig. 11(a) represent the numerical simulation of the equivalent circuit of Fig. 4 for the L_{v2} value. Note that the upper TZ shifts to higher frequencies, and the higher-order mode shifts upward more rapidly than the upper TZ in inverse proportion to L_{v2}. More importantly, this approach preserves desired passband characteristics, such as steep roll-off and ultra-narrowband response, unlike previous studies that required increasing bandwidth to improve out-of-band rejection [17]. This accomplishment eliminates the necessity for additional parametric optimizations. To enhance out-of-band rejection in the upper stopband, reducing L_{v2} is necessary, which can be achieved by increasing the via diameter (d_v) in the full-wave model. The solid lines in Fig. 11(a) represent the EM simulation of the UCs for the d_v. For all d_v values, s_v is 0.9 mm. In line with the circuit simulation for L_{v2}, it is evident that an increase in d_v causes the upper TZ to shift upwards, leading to a notable improvement in out-of-band rejection in the upper band. An

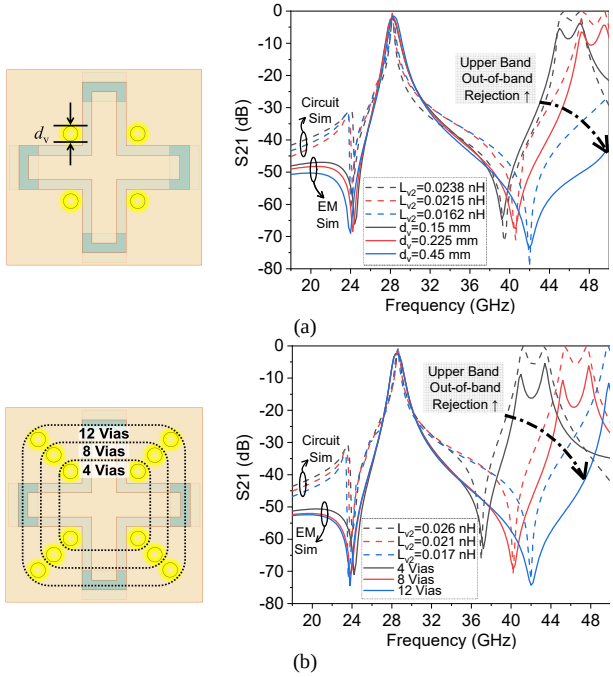

Fig. 11. Simulated $|S_{21}|$ of UCs for (a) via dimeter and (b) parallel via arrangement.

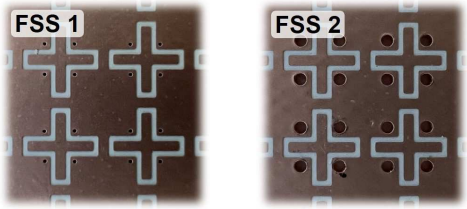

Fig. 12. Fabricated FSSs: (a) d_v=0.15 mm and (b) d_v=0.6 mm.

TABLE III
DESIGN PARAMETERS AND THEIR VALUES IN FIG. 2

l_{l1}	l_{l2}	w_l	p	s_v	d_v	s_a	l_a	w_a	g
0.9	1.3	0.2	4	0.9	0.6	1.65	0.9	0.6	0.05

[Unit: mm]

alternative full-wave modeling involves a parallel arrangement of vias to reduce L_{v2}. As an example, vias are increased diagonally by a factor of 4 to maintain structural symmetry for dual-pol, as shown in the left drawing in Fig. 11(b). d_v of all vias is 0.15 mm. s_v of the four vias closest to the center is 0.6 mm, and the edge-to-edge distance between diagonally arranged vias in each quadrant is 0.13 mm. As depicted in the graphs, the parallel arrangement of a greater number of vias demonstrates a similar effect to increasing d_v.

III. SIMULATION AND MEASUREMENT RESULTS

This section presents both simulated and measured $|S_{21}|$ under TE and TM incidence for each FSS, consisting of two UC samples with varying via inductances. The two different inductances were achieved through the diameter adjustment method. The design parameters and values of the UC 2, which is optimized to improve out-of-band rejection, are specified in Table III. UC 1, which serves as the comparison group shares the same parametric values, except for d_v, which is set to 0.15 mm. Fig. 12(a) and (b) show the photographs of FSS 1 and 2, which are composed of UC 1 and 2, respectively. The FSSs consist of 14×14 UCs, each with lateral dimensions of 56×56 mm^2. The positions of the vias in the two manufactured FSSs deviated

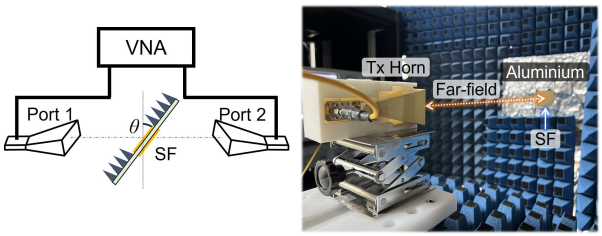

(a) (b)

Fig. 13. FSS measurement (a) schematic and (b) its photograph.

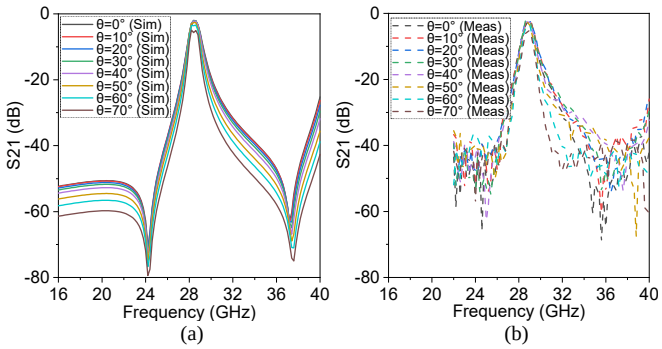

(a) (b)

Fig. 14. (a) Simulated and (b) measured $|S_{21}|$ of FSS 1 with d_v=0.15 mm under TE incidence.

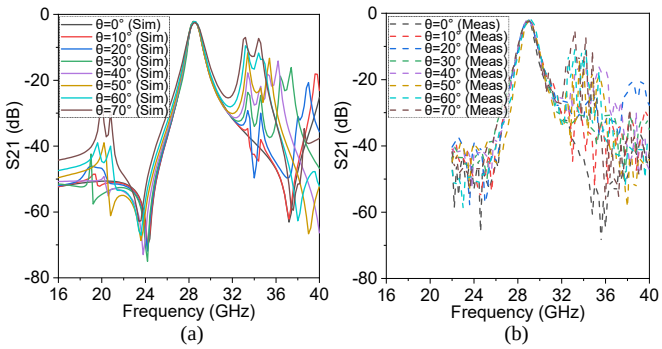

(a) (b)

Fig. 15. (a) Simulated and (b) measured $|S_{21}|$ of FSS 1 with d_v=0.15 mm under TM incidence.

slightly from the intended locations due to a fabrication error as shown in Fig. 12. However, subsequent verification through omitted EM simulations confirmed minimal impact on FSS performance. Fig. 13 shows the measurement schematic and its photograph. A free space measurement setup was constructed with anechoic absorbers. The measurement site consists of 20 dBi gain TRx horns connected to a vector network analyzer (VNA) and a rotating aluminum screen with a central window for FSS installation. The distance between the TRx horns and the FSS was maintained in the far-field. Measurements were conducted in the 22–40 GHz range, considering the WR-28 waveguide cut-off frequencies. $|S_{21}|$ measurement results for FSSs are normalized to the result without FSSs, uninstalled on the central window.

Fig. 14 shows the simulated and measured $|S_{21}|$ of FSS 1 with d_v=0.15 mm under TE incidence. Despite a fabrication error causing an overall frequency deviation of approximately +0.6 GHz, the passband frequency remains stable at incident angles up to 70°, maintaining an exceptionally selective ultra-narrowband response. Minor discrepancies in the stopbands are attributed to fading induced by the wide beamwidth of the TRx horns and spillover effects from the compact size of the prototypes [13]. Fig. 15 shows the $|S_{21}|$ under TM incidence. Likewise, the passband remains stable and the sharp roll-off is well maintained up to 70°. However, $|S_{21}|$ fluctuates significantly and increases as the incident angle rises in both the lower and upper stopbands. Fig. 16 shows the simulated and measured $|S_{21}|$ of FSS 2

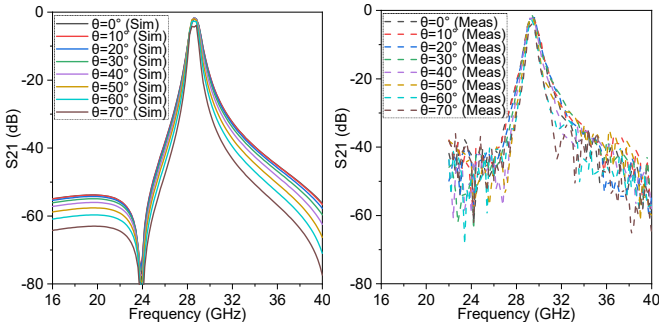

(a) (b)

Fig. 16. (a) Simulated and (b) measured $|S_{21}|$ of FSS 2 with d_v=0.6 mm under TE incidence.

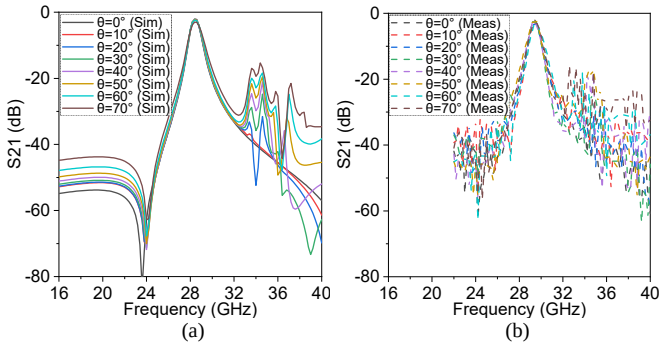

(a) (b)

Fig. 17. (a) Simulated and (b) measured $|S_{21}|$ of FSS 2 with d_v=0.6 mm under TM incidence.

with d_v=0.6 mm under TE incidence. The simulation and measurement results correspond well, demonstrating a significant improvement in out-of-band rejection compared to FSS 1. Fig. 17 shows the $|S_{21}|$ under TM incidence. Note that the degradation of out-of-band rejection in the lower band is eliminated in FSS 2. In addition, the $|S_{21}|$ fluctuation in the upper band improves by more than 10 dB compared to FSS 1. Fig. 18 shows the simulated $|S_{21}|$ of the UCs in Fig. 6 and the finally optimized UC 2. Remarkably, an average out-of-band rejection of 60 dB is achieved across an exceptionally wide frequency range while maintaining an extremely selective ultra-narrowband response.

Table IV presents a comparison between the proposed FSS and existing FSSs based on measured values. The Roll-off for comparing rejection in skirts, is defined as (1), where $f_{3\,\mathrm{dB}}$ represents the 3 dB cut-off frequencies, $f_{5\%}$ represents the skirt frequencies deviating from $f_{3\,\mathrm{dB}}$ by 5% based on the center frequency (f_0), and IL$f_{3\,\mathrm{dB}}$ and IL$f_{5\%}$ correspond to the IL values at $f_{3\,\mathrm{dB}}$ and $f_{5\%}$, respectively.

$$\text{Roll-off} = \left|\mathrm{IL}_{f_{3\,\mathrm{dB}}} - \mathrm{IL}_{f_{5\%}}\right| \ (\mathrm{dB}/\Delta f) \tag{1}$$

The separation percentage is arbitrarily set at 5%, considering the allocated bandwidth of mmWave 5G. The Rejection for comparing out-of-band rejection at the stopband, is defined as (2), where $f_{20\%}$ represents stopband frequencies deviating from $f_{3\,\mathrm{dB}}$ by 20% based on f_0, and IL$f_{20\%}$ corresponds to the IL value at $f_{20\%}$.

$$\text{Rejection} = \left|\mathrm{IL}_{f_{3\,\mathrm{dB}}} - \mathrm{IL}_{f_{20\%}}\right| \ (\mathrm{dB}/\Delta f) \tag{2}$$

A 20% frequency separation from $f_{3\,\mathrm{dB}}$ is chosen to ensure fairness, considering both the measured span for numerical comparison and the out-of-band region with relatively high IL in each counterpart. Δf_0 represents the deviation of f_0 at the maximum reported incident angle compared to normal incidence, while ΔIL indicates the degradation in IL using the same reference. In Roll-off, the proposed FSS shows the highest average rejection for both lower and upper skirts. Furthermore, it demonstrates an unmatched narrowband of 2.7%, comparable to the 800 MHz bandwidth allocated to South Korea's operators and 850

TABLE IV
COMPARISON BETWEEN THE PROPOSED AND PRIOR FSSS (MEASURED VALUE)

Ref	f_0 (GHz)	IL (dB)	Lower/ Upper Roll-off (dB/Δf)	Lower/ Upper Rejection (dB/Δf)	3 dB BW (%)	Angular Stability TE/TM (°)	Δf_0 TE/ TM (%)	ΔIL TE/ TM (dB)
[11]	29.6	1.3	5.7 / 5.8	13.7 / 14.2	4.4	75 / 75	0 / 0	−3 / −1
[12]	21	0.7	22.15 / 15.5	N/A	5	40 / 40	3.8 / 3.3	0 / −1
[13]	3.34	0.5	17.3 / 9.4	11.9 / 24.8	3.7	60 / 60	2.4 / 2.6	−1.5 / 0
[14]	8.9	0.5	8.5 / 2.5	33.9 / 10.35	6.7	20 / 20	1.5 / 1.5	−2 / −2
[15]	5	0.8	5.6 / 8	11.85 / 37.2	5.6	45 / 45	0 / 0	0 / 0
[16]	30	2.8	15.9 / 13.2	N/A	1.7	20 / 20	0 / 0	−2 / −2
[17]	59.5	2.2	25.8 / 11.8	26.3 / 39.3	4	40 / 40	1 / 0.7	−5 / −3.5
his Work	29.3	1.8	21.1 / 18.3	41 / 42.6	2.7	70 / 70	0 / 0	−2.9 / −0.3

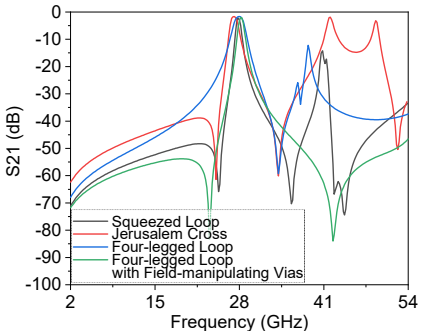

Fig. 18. Simulated $|S_{21}|$ of the UCs in Fig. 6 and the finally optimized UC 2.

MHz bandwidth specified for 5G NR's band n261. Despite achieving a narrower bandwidth in [16] using a fourth-order topology, the IL increases by over 2 dB with a 20° incident angle change, rendering it unsuitable for plug-and-play solutions. In essence, the proposed compact FSS exhibits superior roll-off, higher average out-of-band rejection, ultra-narrowband properties aligned with mmWave 5G bandwidth, and improved angular stability compared to prior studies.

IV. CONCLUSION

This paper presents an ingenious spatial plug-and-play solution for preselector filters. This enhances filtering performance and addresses structural and functional limitations in next-generation miniaturized filters for RFFE, aligning with evolving system architecture demands of compact mmWave base stations. The proposed FSSs utilize high-Q complementary resonator pairs, apertures facilitating mixed coupling paths for TZs, and strategically positioned vias to centralize dominant current, accomplishing unmatchedly selective ultra-narrowband performances with robust angular stability. This technology effectively mitigates interferences in densely deployed mmWave wireless environments with both base stations and reconfigurable intelligent surfaces (RISs). It seamlessly integrates with beamforming modules, significantly enhancing user capacity while providing a cost-effective, power-efficient solution for robust SNR improvement.

REFERENCES

[1] T. S. Rappaport, Y. Xing, G. R. MacCartney, A. F. Molisch, E. Mellios, and J. Zhang, "Overview of millimeter wave communications for fifth-generation (5G) wireless networks—With a focus on propagation models," *IEEE Trans. Antennas Propag.*, vol. 65, no. 12, pp. 6213-6230, Dec. 2017.

[2] J. Kim, W. Lee, and J. Oh, "Liquid-crystal-tuned resonant series patch array with unique element spacing emulating simplified operating construe of traveling-wave antenna," *IEEE Antennas Wireless Propag. Lett.*, Aug. 2023.

[3] J. Kim, J. Kim, J. H. Oh, S.-H. Wi, and J. Oh, "Rotated feed-combined reconfigurable transmit RIS with disparate deployment of 1-bit hybrid units for B5G/6G," *IEEE Trans. Antennas Propag.*, Jun. 2023.

[4] J. Kim, J. H. Oh, S.-H. Wi, and J. Oh, "Asymmetrically layered unit cell topology to reduce cell gap of liquid crystals for 5G millimeter-wave transmissive reconfigurable intelligent surface applications," *IEEE Trans. Antennas Propag.*, Dec. 2023.

[5] K. Lee, J. Kim, E. W. Jin, and K. S. Kim, "Extreme massive MIMO for upper-mid band 6G communications," in *Proc. 13th Int. Conf. Inf. Commun. Technol. Converg. (ICTC)*, Jeju Island, South Korea, Oct. 2022, pp. 997-999.

[6] S. Bastioli, R. V. Snyder, and C. Tomassoni, "Over-moded transverse magnetic cavity filters for narrowband millimeter-wave applications," *IEEE Microw. Wirel. Compon. Lett.*, vol. 29, no. 5, pp. 321-323, May. 2019.

[7] H. Xiao, J. Duan, B. Zhang, A. Zhang, C. Huang, and Q. Jia, "Design and characterization of millimeter-wave micromachined polymer-based cavity filter with resonant cylinders," *Sensors Actuators, A Phys*, vol. 284, pp. 242-250, Dec. 2018.

[8] J. Xu, W. Hong, H. Zhang, and H. Tang, "Compact bandpass filter with multiple coupling paths in limited space for Ku-band application," *IEEE Microw. Wirel. Compon. Lett.*, vol. 27, no. 3, pp. 251-253, Mar. 2017.

[9] G. Shen and W. Che, "Compact Ku-band LTCC bandpass filter using folded dual-composite right-and left-handed resonators," *Electron. Lett.*, vol. 56, no. 1, pp. 17-19, Jan. 2020.

[10] S. Mukherjee and S. K. Mohammed, "How much bandpass filtering is required in massive MIMO base stations?," *IEEE Trans. Veh. Technol.*, vol. 66, no. 5, pp. 4481-4486, Aug. 2016.

[11] H.-H. Chou and G.-J. Ke, "Narrow bandpass frequency selective surface with high level of angular stability at Ka-band," *IEEE Microw. Wirel. Compon. Lett.*, vol. 31, no. 4, pp. 361-364, Apr. 2021.

[12] S. M. A. M. H. Abadi and N. Behdad, "Inductively-coupled miniaturized-element frequency selective surfaces with narrowband, high-order bandpass responses," *IEEE Trans. Antennas Propag.*, vol. 63, no. 11, pp. 4766-4774, Nov. 2015.

[13] W. Afzal, A. Ebrahimi, M. R. Robel, and W. S. Rowe, "Low-profile higher-order narrowband bandpass miniaturized-element frequency-selective surface," *IEEE Trans. Antennas Propag.*, vol. 71, no. 4, pp. 3736-3740, Apr. 2023.

[14] X. Wang, Y. Wang, D. Zhou, D. Lv, and Q. Liu, "High selectivity FSS with three independently controllable transmission poles using matrix synthesis," *IEEE Antennas Wireless Propag. Lett.*, vol. 22, no. 3, pp. 457-461, Mar. 2022.

[15] X. Zhou *et al.*, "A novel design of a compact frequency-selective surface with high selectivity and angular stability," *IEEE Microw. Wirel. Compon. Lett.*, vol. 32, no. 7, pp. 931-934, Jul. 2022.

[16] G. Q. Luo, W. Hong, Q. H. Lai, K. Wu, and L. L. Sun, "Design and experimental verification of compact frequency-selective surface with quasi-elliptic bandpass response," *IEEE Trans. Microw. Theory Techn.*, vol. 55, no. 12, pp. 2481-2487, Dec. 2007.

[17] P. Zhao and C. H. Chan, "Design and analysis of a high-selectivity frequency-selective surface at 60 GHz," *IEEE Trans. Microw. Theory Techn.*, vol. 64, no. 6, pp. 1694-1703, Jun. 2016.

[18] K. Ma, J.-G. Ma, K. S. Yeo, and M. A. Do, "A compact size coupling controllable filter with separate electric and magnetic coupling paths," *IEEE Trans. Microw. Theory Techn.*, vol. 54, no. 3, pp. 1113-1119, Mar. 2006.

[19] H. Wang and Q.-X. Chu, "Generation of transmission zero through electric and magnetic mixed coupling," in *Proc. Int. Conf. Microw. Millim. Wave Technol.*, Apr. 2007, pp. 1-3.

[20] J.-S. Hong and M. J. Lancaster, "Couplings of microstrip square open-loop resonators for cross-coupled planar microwave filters," *IEEE Trans. Microw. Theory Techn.*, vol. 44, no. 11, pp. 2099-2109, Nov. 1996.

[21] J. Oh, "Millimeter-wave thin lens employing mixed-order elliptic filter arrays," *IEEE Trans. Antennas Propag.*, vol. 64, no. 7, pp. 3222-3227, Apr. 2016.

[22] G. Venkatesh, M. Thottappan, and S. P. Singh, "Highly angularly stable dual-band stop FSS for blocking satellite downlink frequencies," *IEEE Trans. Electromagn. Compat.*, vol. 64, no. 6, pp. 2055-2059, Dec. 2022.